RSC Advances

PAPER

View Article Online
View Journal | View Issue

Cite this: *RSC Adv.*, 2015, **5**, 32580

A Surlyn/magnesium oxide nanocomposite as an effective water vapor barrier for organic device encapsulation

Gayathri N. Kopanati,[a] Sindhu Seethamraju,[b] Praveen C. Ramamurthy[bc] and Giridhar Madras*[a]

Received 23rd February 2015
Accepted 31st March 2015

DOI: 10.1039/c5ra03356j

www.rsc.org/advances

A reactive polymer nanocomposite system was proposed as an effective water vapor barrier material for organic device encapsulation. Nanosized magnesium oxide (MgO) was synthesized by the solution combustion technique using two different fuels, lactose and alanine. The purity and crystallite size of MgO were determined from X-ray diffraction studies. The surface areas and porosity measurements were used to determine the water adsorption capacities of MgO. Nanocomposites with various concentrations (wt% = 0.25, 0.5, 1 and 2.5) of MgO were prepared using Surlyn as the base polymer. The permeation rate of moisture through the fabricated films was calculated using calcium degradation test and these rates were further used to calculate the diffusivities. Accelerated aging experiments were conducted to study the performance of organic photovoltaic devices encapsulated with synthesized films under accelerated weathering conditions. The performance of the barrier materials with synthesized MgO was also compared to that obtained with commercial MgO. The films containing MgO obtained from lactose exhibited better barrier properties compared to other films made with commercial MgO and MgO synthesized using alanine as well as other nanocomposites reported in the literature.

1. Introduction

Advancements in the field of organic semiconductor materials and their processing techniques have led to the development of various cost effective organic devices.[1,2] These devices have desirable properties for commercial applications such as a direct band gap, light weight and flexibility. However, the commercialization of these devices still remains a challenge because of the degradation of the active layer device components at ambient atmospheric conditions. Moreover, the hole transporting layers used in these organic devices such as poly(3,4-ethylenedioxythiophene) polystyrene sulfonate (PEDOT:PSS) are highly hygroscopic in nature. These layers absorb moisture and create insulating patches at the layer/electrodes interface.[3–5] Furthermore, oxygen and water vapor also accelerate the photo-degradation resulting in reduced lifetimes and lower efficiencies of the organic devices.[6,7] Therefore, the development of flexible barrier films for organic device encapsulation is of great interest to improve the device stability.

Gas barrier materials have direct applications in the packaging industry for food, pharmaceutical, electronics, *etc.*[8,9] However, organic device encapsulants are required to satisfy the barrier for water vapor with water vapor transmission rates (WVTR) of $<10^{-6}$ g per m^2 per day.[10] Several encapsulation materials such as glass/metal lids and thin polymer films are used conventionally. Though glass and metallic barriers can provide the required barrier for oxygen and water vapor, they are rigid and cannot be used with flexible organic electronics.[10] Thus the development of thin and flexible ultra-high barrier films has gained a lot of interest in the field of encapsulation. Polymer films with multilayered inorganic/organic coatings have been reported in the literature to reduce the WVTR by ~4–5 orders when compared to the neat polymers.[11–13] However, encapsulants with inorganic layers are limited by structural defects like pinholes that promote the diffusion of water vapor and oxygen resulting in poor barrier performance over a period of time. Therefore, inorganic coatings over the polymer substrate do not provide a satisfactory and long term solution for encapsulation. However, the positive effect of inorganic materials such as their reactivity with water molecules could be used to reduce the permeation rates by blending these materials with polymers to form polymer nanocomposites.

Polymer nanocomposites have been widely studied for their superior reinforcement, barrier, electrical and thermoelectric properties.[14–17] The mechanical strength of the polymer is improved by the addition of nanoparticles, which occupy the

[a]*Department of Chemical Engineering, Indian Institute of Science, Bangalore, 560012, India. E-mail: giridhar@chemeng.iisc.ernet.in; Tel: +91 80 22932321*

[b]*Centre for Nanoscience and Engineering, Indian Institute of Science, Bangalore, 560012, India*

[c]*Department of Materials Engineering, Indian Institute of Science, Bangalore, 560012, India*

voids and reduce the propagation of cracks. Therefore, composites with higher mechanical strength and flexibilities are of particular interest for organic device encapsulation applications. Moreover, the nanoparticles in the polymer matrix create a tortuous path for the permeating molecule thereby increasing the diffusion path length and penetration time resulting in decreased permeation rates.[18] These nanoparticles can either react or not react with the incoming permeant. Several non-reactive composites have been previously studied for their water vapor and oxygen barrier properties.[19–22] However, reactive nanocomposites where the nanoparticles are reactive to permeating molecules have not been investigated. Therefore, the reactive nanocomposites that can result in reduced water vapor permeabilities have been synthesized in this work.

The performance of polymer nanocomposites is affected by the type, dispersion, loading and geometry of the nanoparticles.[18,23,24] Though nanoparticles can be synthesized by a wide variety of methods, the solution combustion technique has been used in this study due to its tailorability. This technique is relatively simple and has been extensively used to synthesize metal oxides of various shapes and sizes.[25,26] In this technique, the precursor medium, which is in aqueous state, is subjected to high temperature. The solution ignites and forms the desired product. The aqueous solution helps in the proper mixing of reactants, while high temperatures ensure the purity of the product.[27,28] The particle size, surface area, pore size and defect sites can be controlled by changing the fuel and fuel to oxidizer ratios.[29] The synthesis of magnesium oxide (MgO) by solution combustion using hexamine,[30] starch[31] and glycine[32] as fuels has been reported. However, its synthesis by lactose and alanine has not been studied previously. Further, the possible use of MgO as reactive encapsulant has not been explored.

Therefore, the objective of the work was to synthesize reactive polymer nanocomposites where the nanoparticles are reactive with the permeating molecules. Synthesized MgO was used as the reactive nanoparticle in Surlyn polymer matrix. Surlyn was chosen to be the polymer matrix because of its lower WVTR, chemical resistivity and thermal stability.[33] These polymer nanocomposites were characterized by several techniques to understand the material, mechanical and thermal properties. Further, their ability to withstand humid environmental conditions was studied from water vapor permeability measurements through the barrier films and accelerated aging experiments for encapsulated organic devices.

2. Experiments

2.1 Materials

Magnesium nitrate hexahydrate purified, alanine (A), and dichlorobenzene were procured from S.D Fine chemicals Ltd. (India). Lactose (L) was obtained from Fischer Scientific. Surlyn (zinc salt) was purchased from Aldrich Chemical Company, Inc. (USA). PEDOT–PSS, [6,6]-phenyl-C_{61}-butyric acid methyl ester (PCBM) and calcium metal (~99.99% purity) were procured from Sigma Aldrich Co. (USA). Poly(3-hexylthiophene) (P3HT) was obtained from Rieke Metals Inc. (USA). The epoxy glue used for sealing the barrier films was purchased from Atul Industries Ltd. (India). Commercial MgO (C-MgO) was obtained from Merck & Co. (USA).

2.2 Sample preparation

MgO was synthesized following the solution combustion process. Aqueous solutions of magnesium nitrate (6.4 g) and the fuels in their respective stoichiometric molar ratios were mixed. The stoichiometric amounts were calculated based on the oxidizer to fuel molar ratios, which are 0.67 and 0.21 for alanine and lactose, respectively. These aqueous solutions were then placed in a furnace maintained at 350 °C for ~20 min, separately. The mixtures were combusted at this temperature to form a powder of MgO. The products formed from alanine were white in color whereas the products from lactose were brown in color. Therefore, the product obtained from lactose was calcined for 2 h at 400 °C that resulted in a white powder. The calcined and uncalcined products of lactose are tagged as CL-MgO and UL-MgO, respectively. Similarly, the product from alanine is referred as A-MgO. The synthesized MgO was melt mixed with Surlyn in a twin screw extruder (Haake Mini Lab) at 180 °C and 100 rpm. The samples were prepared by varying the weight percent of MgO (0.25, 0.5, 1 and 2.5 wt%) in Surlyn to study the effect on barrier properties. The same procedure was repeated for C-MgO also. The extruded samples were compressed at a temperature of 180 °C and a pressure of 10 kN using a hydraulic press. The films (~100 μm) thus obtained were further used for characterization and permeability studies.

2.3 Characterization methods

The crystallite size of MgO particles was determined using Rigaku X-ray diffractometer (XRD) at a scan rate of 1° min^{-1} over a 2θ range of 25–85°. The surface areas and pore volumes of synthesized MgO were determined using Smart sorb 92/93 BET instrument. Water vapor absorption isotherms and BET surface areas for water vapor adsorption were obtained from Belsorp-Max and Belsorp-Aqua Porosimeter, respectively. The mechanical properties of the barrier films were determined using Mecmeisin Micro Universal Testing Machine, with 10 kN load cell at a rate of 25 mm min^{-1} following ASTM D882-12. Perkin Elmer (Lambda 35) UV-visible spectroscope was used to determine the transparency of films.

2.4 Permeability studies

WVTR was determined by following the calcium degradation test. A neat, cleansed glass slide (2 × 2 cm) was taken and calcium was deposited at the centre of the glass slide with dimensions of 1 cm in length (l) and 1 cm in breadth (b) in a thermal evaporator under ultra-high vacuum. The thickness of the deposited calcium was ~200 nm. Aluminium was then evaporated on either side of calcium such that it is in contact with the deposited calcium. Thus the deposited aluminium acts as electrodes. The calcium was completely covered and sealed with the fabricated films using an epoxy sealant. A Kaleidoscope humidity chamber was used to maintain humid conditions of relative humidity (RH) ~ 95% at a temperature of 35 °C. The

calcium deposited glass slides sealed with the fabricated barrier films were placed in the humidity chamber exposing them to humid atmosphere. The moisture permeating through the barrier films reacts with calcium, resulting in the increase of calcium thin film resistance with time. Digital multimeter was used to record these changes of resistance (R) with time (t). The WVTR through the barrier films was further calculated from the data obtained using eqn (1).[11]

$$\mathrm{WVTR} = -2\,\frac{M_{\mathrm{H_2O}}}{M_{\mathrm{Ca}}}\,\delta\rho(l/b)\,\frac{\mathrm{d}(1/R)}{\mathrm{d}t} \qquad (1)$$

In eqn (1), $M_{\mathrm{H_2O}}$ and M_{Ca} are the molecular weights of H_2O and calcium. The above equation is applicable only when resistivity (ρ) of calcium is constant and can be considered above 100 nm thickness of calcium.[34] Therefore, only the data between 200 nm to 100 nm was considered in the calculations.

2.5 Aging studies

Standard organic photovoltaic devices (OPVD) were prepared using indium–tin oxide (ITO) coated glass slides. The edges of these glass slides were properly etched such that the ITO was present only at the centre. The etching was followed by spin coating of PEDOT–PSS at 3000 rpm for 1 min. The spin coated glass slides were annealed at 110 °C for 10 min. These glass slides were further spin coated with solution of P3HT (22 mg) and PCBM (18 mg) in 1 mL of dichlorobenzene at 1000 rpm for 1 min and were annealed at 140 °C for 10 min. Aluminum (electrodes) was thermally evaporated onto the glass slide. The OPV devices were then hermetically sealed with the fabricated barrier films using epoxy glue. The sealed devices were then subjected to accelerated weathering conditions of RH ~ 85% and 65 °C.[35] Keithley semiconductor characterization system (4200) and the solar simulator (sol 3 A, Newport Oriel) were used to measure the efficiencies of the encapsulated devices before and after aging.

3. Results and discussion

3.1 MgO characterization

The synthesized MgO is used as reactive nanoparticle in Surlyn to decrease WVTR. The presence of MgO nanoparticles in the Surlyn matrix increases the diffusion path length and results in lower WVTR. Further, the water molecules permeating through the matrix are reactive to MgO,[36] which would further decrease the permeation rates. The reactivity of moisture on MgO depends on various factors such as the size of the particles, surface area, aspect ratio, defect sites and carbon content. Therefore, the synthesized MgO, A-MgO, UL-MgO, CL-MgO and the commercial MgO (C-MgO) were characterized using XRD and BET surface area analyzer.

3.2 XRD

MgO obtained from solution combustion and commercially were characterized using XRD and the diffraction patterns are given in the Fig. 1. The diffraction peaks at 36.9°, 42.9°, 62.3°, 74.7° and 78.6° are characteristic of MgO that confirms that a pure product is obtained from the combustion synthesis. The peak at 36.9° corresponds to the 111 plane while the peak at 42.9° corresponds to the 200 plane of MgO. The small visible peaks for 111 planes suggest the presence of higher defects and larger number of microfaceted steps.[37] The ratios of intensities of 200 to 111 planes for CL-MgO, UL-MgO, C-MgO and A-MgO are 14, 17, 39 and 63, respectively. The lowest ratios were obtained for MgO synthesized from lactose when compared to the MgO obtained from alanine suggesting the presence of higher defect sites. The crystallite size was further obtained using the diffraction pattern that was determined by the Scherrer formula.[38] The crystallite sizes of UL-MgO, CL-MgO, A-MgO and C-MgO obtained from the full width half maximum of 200 peak were found to be 5, 6, 14 and 10 nm (Table 1), respectively. Thus the MgO synthesized from lactose has the least crystallite size and higher defect sites when compared to the commercial MgO and MgO synthesized with alanine.

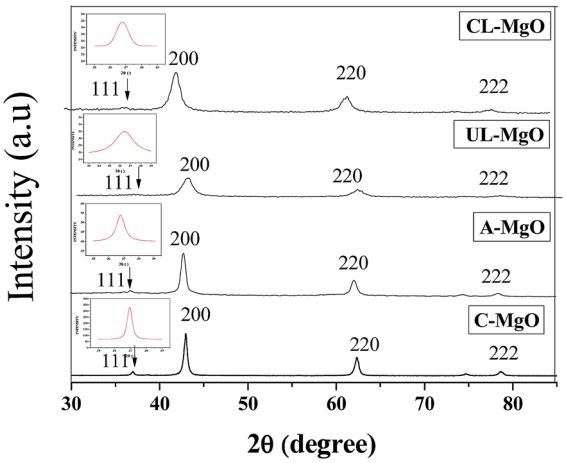

Fig. 1 XRD pattern of MgO obtained from different fuels and commercially obtained MgO, inset: magnified view of 111 peaks.

3.3 Surface area analysis

The surface areas for the synthesized and commercial MgO were determined from the nitrogen adsorption–desorption BET surface area analysis. The surface areas for A-MgO, CL-MgO, UL-MgO and C-MgO were found to be 12.0, 46.8, 52.2 and 43.2 $m^2\ g^{-1}$ as given in Table 1, respectively. The high surface areas exhibited by UL-MgO and CL-MgO can be attributed to their lower crystallite sizes. The surface area for MgO synthesized from alanine is the lowest due its larger crystallite size. The pore volumes determined from BET analysis were ~0.001 $cm^3\ g^{-1}$ for A-MgO, 0.03 $cm^3\ g^{-1}$ for both UL-MgO and CL-MgO and ~0.1 $cm^3\ g^{-1}$ for C-MgO. This shows that the MgO synthesized using alanine as the fuel has the least pore volumes, which is 30 times lower than the MgO synthesized from lactose. Based on these results, the synthesized MgO and commercial MgO were subjected to water vapor adsorption–desorption BET surface area experiments. The water vapor adsorption surface areas were found to be 28, 30, 83 and 113 $m^2\ g^{-1}$ for A-MgO, C-MgO, CL-MgO and UL-MgO,

Table 1 Surface area and barrier properties of synthesized MgO and MgO composite films. The surface area and pore volume are based on nitrogen absorption–desorption

Fuel	Crystallite size (nm)	Surface area ($m^2\ g^{-1}$)	Pore volume ($cm^3\ g^{-1}$)	Water adsorption capacity ($m^2\ g^{-1}$)	WVTR at 3000 s (1% loading of MgO) (g per m^2 per day)	Device performance% efficiency retained (1 h under accelerated aging conditions)
UL-MgO	5	52.2	0.030	113	0.008	40
CL-MgO	6	46.8	0.030	83	0.015	26
A-MgO	14	12.0	0.001	28	0.030	22
C-MgO	10	43.2	0.100	30	0.028	20

respectively. Therefore, the MgO synthesized from lactose exhibited the highest water vapor adsorption capability, which is at least 2.5 times higher than MgO synthesized with alanine. Further, the mono-layer adsorption capacity for UL-MgO was found to be 33 $cm^3\ g^{-1}$ that is higher by 2.3 times when compared to that for A-MgO (14 $cm^3\ g^{-1}$). The commercial MgO exhibited the least mono-layer adsorption capacities with 9 $cm^3\ g^{-1}$. These results suggest the importance of the process of synthesis of the nanomaterials for obtaining varying characteristics resulting in different properties.

3.4 Film characterization

The nanocomposite films were fabricated using Surlyn and MgO from synthesis and commercial sources. These films were subjected to mechanical and barrier analyses to validate their suitability for flexible encapsulation applications. Accelerated encapsulated OPV device aging studies further provide the evidence for real time applicability of the fabricated barrier films.

3.5 Mechanical properties

The barrier films employed for encapsulation of organic devices have to be flexible and also be capable of withstanding mechanical load and stress. Hence, mechanical properties of encapsulant films are critical for this study. The fabricated films were tested for their mechanical stabilities and shown in Fig. 2. The tensile strength of the films increased with the increase in nanoparticle concentrations (Fig. 2(a)). The films with commercial MgO exhibited the least strength at all the loadings when compared to the films with synthesized MgO. This further shows that the method of synthesis plays an important role on the resultant properties, as discussed previously. The profile for tensile strengths shows that the particle size of the nanoparticle affects the resultant tensile properties. When the particle size of the nanomaterial is smaller, the tensile strength of the composite films is higher. The crystallite sizes were observed to be the lower for UL/CL-MgO and highest for A-MgO. Therefore, the tensile strength is the highest for the composites with UL-MgO and lowest for composites with A-MgO when compared among the synthesized MgO composites.

The tensile strength is higher for Surlyn/UL-MgO (7.5 ± 2 MPa) and Surlyn/CL-MgO (7.2 ± 2 MPa) at 2.5% of MgO when compared to all the other nanocomposites and neat Surlyn film (3.6 ± 2 MPa). A similar trend was observed for Young's modulus of the composites (Fig. 2(b)) with the nanocomposites exhibiting higher modulus compared to neat Surlyn (93 ± 2 MPa). These results show that the films with synthesized MgO from lactose show better mechanical properties than the other composites. The elongation at break decreased with the increasing of the nanoparticle loading in the nanocomposite (Fig. 2(c)). It was least for Surlyn/UL-MgO (63 ± 2%) compared to other nanocomposites and neat Surlyn film (135 ± 3%). All of the nanocomposites films exhibited elongations at break >70%. Therefore, these films are suitable for flexible applications.

3.6 Optical properties

The optical properties of all the nanocomposite films and neat Surlyn film were studied using UV-visible spectral analysis over the range of 1100–230 nm. The UV-visible spectrum for Surlyn/UL-MgO is given in Fig. 3(a). The average transmittance in the visible region is ~82, 77, 67 and 50% for 0.25, 0.5, 1 and 2.5% of UL-MgO loading in Surlyn. Further, the average transmittance of all the nanocomposite films was determined using the spectrum and is given in Fig. 3(b). It can be observed from both the data that the transmittance decreases with an increase in the filler concentration. The neat film has an average transmittance of ~84% whereas the composites exhibited >65% transmittance explicitly in the visible region, which is higher than the traditional glass with EVA module.[37] Moreover, the addition of MgO to Surlyn improved the UV barrier by decreasing the transmission in the UV region. Therefore, the fabricated composite films are suitable for encapsulating OPV devices.

3.7 Reactivity of MgO with water vapor

The synthesized MgO powder was placed in a humidity chamber maintained at relative humidity of 95% and temperature of 35 °C (similar to the conditions for calcium degradation test) for 2 h. The obtained powder was characterized by XRD. The diffraction pattern of the sample is given below (Fig. 4). The diffraction peaks at $2\theta = 38.2$, 50.9, 58.7, 62.2, 68.4, 72.03 and 81.5° are characteristic peaks of magnesium hydroxide (JCPDS: 001-1169). This indicates that MgO placed in the humid atmosphere is capable of reacting with moisture resulting in the formation of $Mg(OH)_2$. Thus, Surlyn/MgO will act as a reactive nanocomposite in the presence of moisture.

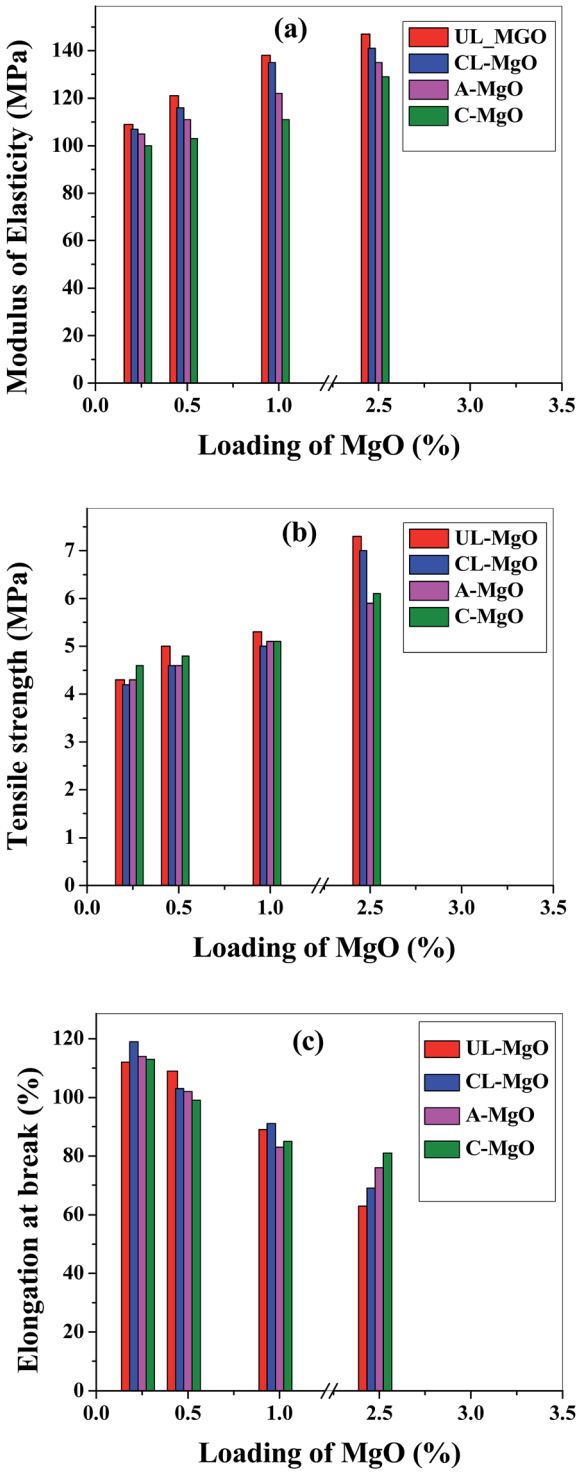

Fig. 2 (a) Modulus of elasticity (b) tensile strength and (c) elongation at break for fabricated composite films.

3.8 Permeability studies

The water vapor barrier properties of the fabricated films have been determined from calcium degradation test (at RH ~ 95% and 35 °C). Fig. 5(a) shows the WVTRs calculated for the Surlyn/MgO nanocomposites at ~3000 s. It can be inferred from these results that the loading of MgO affects the water vapor

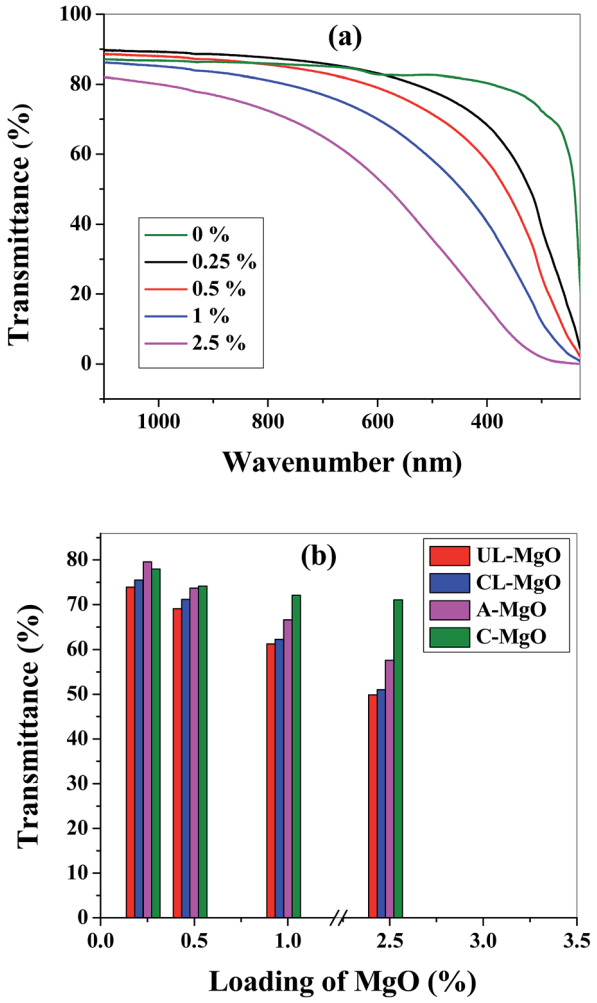

Fig. 3 (a) UV-visible spectrum for Surlyn/UL-MgO nanocomposite for different MgO loadings (b) average transmittance of synthesized nanocomposite films with different MgO loading, determined from UV-visible spectrometer.

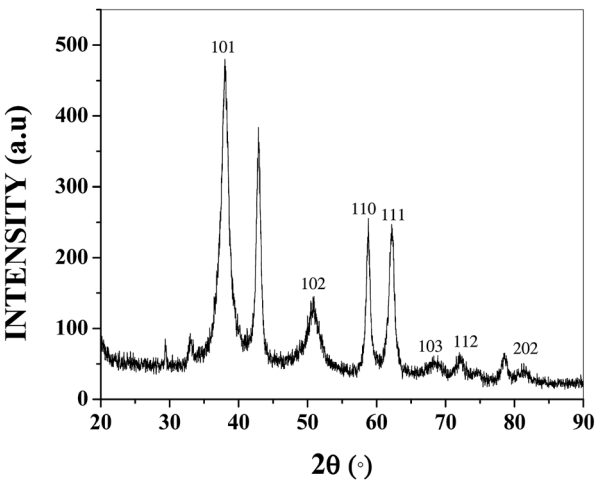

Fig. 4 Diffraction pattern of magnesium hydroxide.

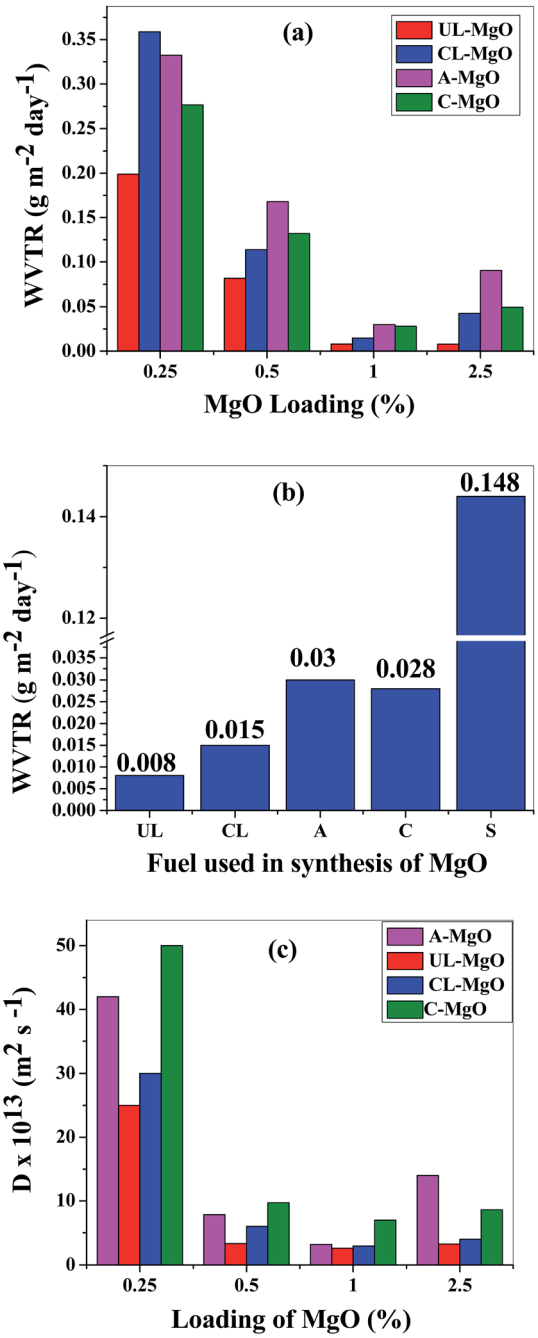

Fig. 5 (a) WVTR of Surlyn/MgO for different precursors used in combustion synthesis of MgO and for different compositions of MgO (b) WVTR (c) diffusivities (D) of Surlyn/MgO nanocomposite at 1% loading compared with neat Surlyn (S).

permeability. The WVTRs decreased from 0.25 to 1% loadings of MgO in Surlyn. However, there is an increase in WVTR for 2.5% loading of MgO which could be due to the agglomeration of MgO and decreased diffusion path lengths. Thus there is an optimum concentration of nanoparticles, which exhibit better barrier properties compared to other concentrations. Therefore, the optimum loading of MgO is ~1% irrespective of the fuel used for the synthesized composites. On comparing the reactivity of MgO obtained from two different fuels (Fig. 5(b)), it is found that the WVTR for Surlyn/UL-MgO (0.008 g per m^2 per day) at 1% loading exhibited the least values. The WVTRs for other composites, Surlyn/CL-MgO (0.015 g per m^2 per day), Surlyn/A-MgO (0.030 g per m^2 per day) and Surlyn/C-MgO (0.028 g per m^2 per day) showed no significant difference at 1% loading (Table 1). However, the films with UL-MgO and CL-MgO showed lower water vapor permeabilities compared to the other composites due to their better dispersion and higher surface areas. The WVTR through the Surlyn/UL-MgO film decreased by ~50% than that of Surlyn/CL-MgO. This reduction is due to the presence of carbonaceous impurities in UL-MgO, which were removed by calcination in CL-MgO. In order to verify carbonaceous impurities, thermogravimetric analysis was carried out for UL-MgO and CL-MgO in the presence of oxygen. The weight loss of ~30% was observed between 300 and 400 °C indicating the presence of carbonaceous impurities. Therefore, the synergistic effect of high surface area and defect sites in UL-MgO results in a lower WVTR compared to Surlyn/CL-MgO and Surlyn/A-MgO films.

The reduction in WVTR in the films with MgO is due to the reactivity of MgO and the increased diffusion path for permeation. Therefore, the diffusivities of water vapor through the fabricated films were determined and calculated using eqn (2).[19]

$$\frac{Q}{sc} = \frac{Dt}{s^2} - \frac{1}{6} - \frac{2}{\Pi^2}\sum_{n=1}^{\alpha}\left[\frac{-1^n}{n^2}\exp\left(\frac{-Dn^2\Pi^2 t}{s^2}\right)\right] \quad (2)$$

In eqn (2), Q is the cumulative WVTR obtained from calcium degradation test, s is the thickness of the film, c is the concentration of moisture at 95% RH and 35 °C, D is the diffusivity and t is the time. The diffusivities of water vapor through these films decreased by one order when compared to neat Surlyn film. It can be observed from Fig. 5(c) that the diffusivities decrease with increasing MgO loading from 0.25% to 1% and increase for loadings from 1% to 2.5%. Further, the lowest diffusivity was observed for Surlyn/UL-MgO nanocomposite at 1% loading of MgO.

Therefore, the WVTR and diffusivity calculations show that 1% of MgO is the optimal loading for water vapor barrier properties above which agglomeration of the nanoparticles results in a decreased diffusion path resulting in higher WVTR. Such observations regarding optimal loading of nanoparticles for WVTR have been previously reported for functionalized[20] and mesoporous[38] silica and clay.[39]

3.9 Device performance studies

The normalized efficiencies of OPVDs are given in Fig. 6. The OPVDs were encapsulated with the fabricated films and exposed to accelerated weathering conditions of 85% RH and 65 °C for 1 h. The efficiencies were normalized with their respective initial efficiencies (efficiencies at time = 0). The unencapsulated device did not sustain and lost all of its efficiency in 10 min. The device encapsulated with neat Surlyn retained ~8% of its initial efficiency after 1 h of accelerated aging, while the highest retained efficiency was observed for device encapsulated with Surlyn/UL-

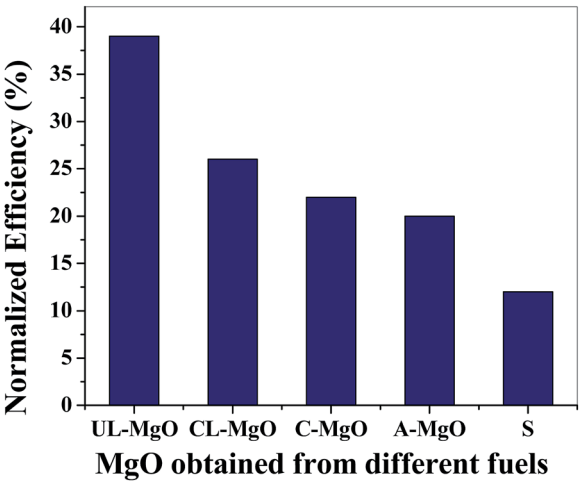

Fig. 6 Normalized efficiencies of OPV devices encapsulated with fabricated films with MgO nanoparticles, obtained from different precursor medium, after 1 h exposure to accelerated weathering conditions.

MgO film. It retained ~40% efficiency even after 1 h of exposure to accelerated weathering conditions (Table 1). The OPVDs encapsulated with Surlyn/CL-MgO retained efficiencies of ~26%, followed by the OPVDs encapsulated with C–MgO and A-MgO with retained efficiencies ~20 and 22%, respectively. Therefore, the water vapor permeability results and the accelerated weathering studies are in agreement following the same trend.

4. Summary and conclusions

The OPVDs encapsulated with reactive Surlyn/UL-MgO nanocomposite films were observed to retain their efficiencies for longer times when subjected to accelerated weathering conditions. These films also exhibited lower WVTR and water vapor diffusivities compared to the neat Surlyn films. The MgO nanoparticles incorporated in Surlyn matrix improved the water vapor barrier properties due to the higher diffusion path lengths and chemical reactivity to H_2O molecules.[36]

The least permeability is shown by Surlyn/UL-MgO followed by composites with CL-MgO, C-MgO and A-MgO (Table 1). The reactivity of these nanoparticles depends on various factors such as surface area, defect sites, particle size and carbonaceous content. The solution combustion technique resulted in products with larger defect sites that can increase the reactivity of nanoparticles. The exposure of the 111 plane is higher for UL-MgO compared to other synthesized and commercial MgO. This plane is the stepped surface of MgO and shows higher adsorption of water molecules.[32] Moreover, the pore volumes are higher for CL/UL-MgO. Therefore, the Surlyn films blended with UL-MgO exhibited better barrier properties compared to neat and other nanocomposite films. Moreover, the device encapsulated with UL-MgO retained an efficiency of ~40%, even after 1 h of exposure to accelerated weathering conditions, suggesting better barrier properties. Table 1 shows that UL-MgO has the lowest crystallite size, higher surface area, largest water absorption capacity and larger defect sites compared to other MgO synthesized in this study. This leads to the best barrier properties for Surlyn/UL-MgO composite films.

Previously investigated barrier materials with different nanoparticles such as zinc oxide, functionalized silica and amine functionalized alumina exhibited up to 2 orders lower WVTRs than the neat polymers (Table 2). The WVTRs obtained from zinc oxide, clay and functionalized alumina are comparable to the WVTR from MgO nanocomposite. However, the amount of nanoparticles used in this study is comparatively lower than the other studies. The fabricated barrier films also exhibited lower WVTR for a longer period of time compared to other materials. The WVTR of Surlyn/MgO composite at 1% loading of MgO is 20 000 times better than the neat Surlyn film. The mechanical, barrier and aging characterizations for the fabricated Surlyn/MgO composites show that they are suitable for encapsulating OPVDs. The use of reactive component, MgO in Surlyn, resulted in better water vapor barrier. Therefore, the fabricated Surlyn nanocomposite system with synthesized MgO is effective as water vapor barrier for encapsulating organic electronic devices and is better than the existing state-of-the-art materials.

This work shows that the reactive nanocomposite system can significantly reduce the water vapor permeability. Therefore, future work can further explore the various branched polymers and reactive nanomaterials, which are generally used for sensing, catalytic and reactive applications for designing better moisture barrier materials for organic device encapsulation applications.[40–43]

Acknowledgements

The authors would like to acknowledge the financial support for this project from SERB, Department of Science and Technology (1362/2014) and IUSSTF/JCERDC-SERIIUS/2012 dated 22nd Nov. 2012.

Table 2 Comparison of WVTRs for different filler materials calculated at RH: 95% and temperature: 35 °C

Polymer	Inorganic filler	Loading (%)	Time (s)	WVTR (g per m^2 per day)	Thickness (μm)	Reference
Poly(vinyl butyral)	Functionalized silica	1.5	200–800	0.07	200	20
Polyvinyl alcohol	Zinc oxide	4	150–200	0.0088	250	21
Poly(vinyl butyral)	Alumina	4	1000–1500	0.015	250	19
Poly(vinyl butyral)	Functionalized alumina	5	1000–1500	0.002	250	19
Cyclic olefin copolymer	Clay	4	12 000–15 000	0.004	75	39
Surlyn	MgO	1	0–3300	0.008	150	This study

References

1 P. C. Ramamurthy, W. R. Harrell, R. V. Gregory, B. Sadanadan and A. M. Rao, *J. Electrochem. Soc.*, 2004, **151**, G502–G506.
2 P. C. Ramamurthy, W. R. Harrell, R. V. Gregory, B. Sadanadan and A. M. Rao, *Polym. Eng. Sci.*, 2004, **44**, 28–33.
3 N. Grossiord, J. M. Kroon, R. Andriessen and P. W. Blom, *Org. Electron.*, 2012, **13**, 432–456.
4 E. Voroshazi, I. Cardinaletti, T. Conard and B. P. Rand, *Adv. Energy Mater.*, 2014, **4**, 1400848, DOI: 10.1002/aenm.201400848.
5 A. Seemann, H.-J. Egelhaaf, C. J. Brabec and J. A. Hauch, *Org. Electron.*, 2009, **10**, 1424–1428.
6 F. C. Krebs, J. E. Carlé, N. Cruys-Bagger, M. Andersen, M. R. Lilliedal, M. A. Hammond and S. Hvidt, *Sol. Energy Mater. Sol. Cells*, 2005, **86**, 499–516.
7 A. Sharma, S. E. Watkins, D. A. Lewis and G. Andersson, *Sol. Energy Mater. Sol. Cells*, 2011, **95**, 3251–3255.
8 S. W. Kim and S. H. Cha, *J. Appl. Polym. Sci.*, 2014, **131**, 40289, DOI: 10.1002/app.40289.
9 D. N. Bikiaris and K. S. Triantafyllidis, *Mater. Lett.*, 2013, **93**, 1–4.
10 P. Burrows, V. Bulovic, S. Forrest, L. Sapochak, D. McCarty and M. Thompson, *Appl. Phys. Lett.*, 1994, **65**, 2922–2924.
11 S. Seethamraju, P. C. Ramamurthy and G. Madras, *Appl. Phys. Lett.*, 2014, **105**, 104102, DOI: 10.1063/1.4895719.
12 W. J. Kim, W. H. Koo, S. J. Jo, C. S. Kim, H. K. Baik, J. Lee and S. Im, *Appl. Surf. Sci.*, 2005, **252**, 1332–1338.
13 Z. Wu, L. Wang, C. Chang and Y. Qiu, *J. Phys. D: Appl. Phys.*, 2005, **38**, 981.
14 M. Martinez-Sanz, M. A. Abdelwahab, A. Lopez-Rubio, J. M. Lagaron, E. Chiellini, T. G. Williams, D. F. Wood, W. J. Orts and S. H. Imam, *Eur. Polym. J.*, 2013, **49**, 2062–2072.
15 C. Bora, P. Gogoi, S. Baglari and S. K. Dolui, *J. Appl. Polym. Sci.*, 2013, **129**, 3432–3438.
16 G. P. Moriarty, S. De, P. J. King, U. Khan, M. Via, J. A. King, J. N. Coleman and J. C. Grunlan, *J. Polym. Sci., Part B: Polym. Phys.*, 2013, **51**, 119–123.
17 S. Konwer, R. Boruah and S. K. Dolui, *J. Electron. Mater.*, 2011, **40**, 2248–2255.
18 R. K. Bharadwaj, *Macromolecules*, 2001, **34**, 9189–9192.
19 S. Saravanan, S. Gupta, P. C. Ramamurthy and G. Madras, *Polym. Compos.*, 2014, **35**, 1426–1435.
20 S. Gupta, S. Seethamraju, P. C. Ramamurthy and G. Madras, *Ind. Eng. Chem. Res.*, 2013, **52**, 4383–4394.
21 S. Gupta, S. Sindhu, K. A. Varman, P. C. Ramamurthy and G. Madras, *RSC Adv.*, 2012, **2**, 11536–11543.
22 J. C. Grunlan, A. Grigorian, C. B. Hamilton and A. R. Mehrabi, *J. Appl. Polym. Sci.*, 2004, **93**, 1102–1109.
23 P. Tzeng, C. R. Maupin and J. C. Grunlan, *J. Membr. Sci.*, 2014, **452**, 46–53.
24 J.-I. Weon and H.-J. Sue, *Polymer*, 2005, **46**, 6325–6334.
25 K. Nagaveni, M. Hegde, N. Ravishankar, G. Subbanna and G. Madras, *Langmuir*, 2004, **20**, 2900–2907.
26 K. Nagaveni, M. Hegde and G. Madras, *J. Phys. Chem. B*, 2004, **108**, 20204–20212.
27 M. S. Hegde, G. Madras and K. C. Patil, *Acc. Chem. Res.*, 2009, **42**, 704–712.
28 A. S. Mukasyan, P. Epstein and P. Dinka, *Proc. Combust. Inst.*, 2007, **31**, 1789–1795.
29 P. Erri, J. Nader and A. Varma, *Adv. Mater.*, 2008, **20**, 1243–1245.
30 S. Balamurugan, L. Ashna and P. Parthiban, *J. Nanotechnol.*, 2014, **2014**, 841803, DOI: 10.1155/2014/841803.
31 J. Bai, F. Meng, C. Wei, Y. Zhao, H. Tan and J. Liu, *Ceram.-Silik.*, 2011, **55**, 20–25.
32 B. Nagappa and G. Chandrappa, *Microporous Mesoporous Mater.*, 2007, **106**, 212–218.
33 S. Seethamraju, P. C. Ramamurthy and G. Madras, *ACS Appl. Mater. Interfaces*, 2013, **5**, 4409–4416.
34 P. Renucci, L. Gaudart, J. Petrakian and D. Roux, *Phys. Rev. B: Condens. Matter Mater. Phys.*, 1982, **26**, 5416.
35 M. O. Reese, S. A. Gevorgyan, M. Jørgensen, E. Bundgaard, S. R. Kurtz, D. S. Ginley, D. C. Olson, M. T. Lloyd, P. Morvillo, E. A. Katz, A. Elschner, O. Haillant, T. R. Currier, V. Shrotriya, M. Hermenau, M. Riede, K. R. Kirov, G. Trimmel, T. Rath, O. Inganäs, F. Zhang, M. Andersson, K. Tvingstedt, M. Lira-Cantu, D. Laird, C. McGuiness, S. Gowrisanker, M. Pannone, M. Xiao, J. Hauch, R. Steim, D. M. DeLongchamp, R. Rösch, H. Hoppe, N. Espinosa, A. Urbina, G. Yaman-Uzunoglu, J.-B. Bonekamp, A. J. J. M. van Breemen, C. Girotto, E. Voroshazi and F. C. Krebs, *Sol. Energy Mater. Sol. Cells*, 2011, **95**, 1253–1267.
36 E. S. Cho, C. M. Evans, E. C. Davidson, M. L. Hoarfrost, M. A. Modestino, R. A. Segalman and J. J. Urban, *ACS Macro Lett.*, 2015, **4**, 70–74.
37 K. R. McIntosh, J. N. Cotsell, J. S. Cumpston, A. W. Norris, N. E. Powell and B. M. Ketola, *Photovoltaic Specialists Conference (PVSC), 2009 34th IEEE*, 2009.
38 S. Saravanan, P. C. Ramamurthy and G. Madras, *Compos. Sci. Technol.*, 2014, **96**, 80–87.
39 S. Saravanan, P. C. Ramamurthy and G. Madras, *Composites, Part B*, 2015, **73**, 1–9.
40 S. G. Roy and P. De, *Polym. Chem.*, 2014, **5**, 6365–6378.
41 S. G. Roy, K. Bauri, S. Pal and P. De, *Polym. Chem.*, 2014, **5**, 3624–3633.
42 V. Subramanian, J. Choi, E. Seebauer and R. Masel, *Catal. Lett.*, 2007, **113**, 13–18.
43 B. Mukherjee, W. Wilson and V. R. Subramanian, *Nanoscale*, 2013, **5**, 269–274.